



An efficient Z-type CeO₂/BiOBr heterostructure with enhanced photo-oxidation degradation of o-DCB and CO₂ reduction ability

Juanjuan Sun^{a,b}, Yuxuan Zhang^a, Shiyong Fan^b, Xinyong Li^{b,*}, Qidong Zhao^c

^a College of Marine and Environmental Sciences, Tianjin University of Science & Technology, Tianjin 300457, China

^b State Key Laboratory of Fine Chemicals, Key Laboratory of Industrial Ecology and Environmental Engineering (MOE), School of Environmental Science and Technology, Dalian University of Technology, Dalian 116024, China

^c School of Chemical Engineering, Dalian University of Technology, Panjin 124221, China

ARTICLE INFO

Keywords:

Z-type heterostructures
Photo-oxidation Cl-VOC
CO₂ conversion
Z-scheme mechanism
The charge transfer dynamics

ABSTRACT

The Z-type CeO₂/BiOBr heterostructures were skilfully designed by assembling CeO₂ nanoparticles onto the surface of BiOBr microflowers. This composite photocatalyst demonstrates efficient photo-oxidation degradation ability for o-DCB and CO₂ reduction ability. Through analyses of its morphology, microstructure, XPS spectra, low-temperature ESR, SPV, and charge transfer dynamics (TPV and TR-PL), the paper elucidates the superior performance of the CeO₂/BiOBr composite and discusses its photocatalytic mechanism. The enhanced photo-oxidation degradation ability and CO₂ reduction performance of the heterostructure, compared to the individual CeO₂ and BiOBr components, indicate that this Z-scheme microstructure effectively promotes the recombination of photogenerated holes the valence band (VB) of the BiOBr with the electrons in the conduction band (CB) of the CeO₂, leading to the abundant carriers surviving in the corresponding energy bands. This study provides valuable insights into the rational design of Z-type heterostructures for advanced photocatalytic applications.

1. Introduction

In recent years, the photocatalytic reduction of CO₂ into useful hydrocarbons has emerged as a promising method for addressing energy shortages and mitigating global warming. Besides, the photocatalytic method holds great potential in solving environmental pollution [1]. Various semiconductors such as TiO₂ [2], WO₃ [3], g-C₃N₄ [4], ZnO [5], and SrTiO₃ [6] have been explored as potential photocatalysts. However, the efficiency of single photocatalysts remains unsatisfactory due to the slow separation and transfer kinetics of photogenerated electrons and holes [7,8].

To address this challenge, the construction of heterojunctions with other semiconductors has been proposed to improve the separation efficiency of photoexcited charge carriers [9,10]. While common type II heterojunction systems have been effective, they suffer from weakened redox capacity of the photoexcited electrons and hole pairs due to band gap energy level matching. In contrast, elaborate Z-scheme systems have shown promise in photocatalytic degradation, H₂O splitting and CO₂ reduction [11,12]. In a Z-scheme system, the photoexcited electrons transfer between different semiconductor catalysts, allowing

simultaneous oxidation and reduction capabilities to persist on different materials, resulting in high quantum efficiency under optimal conditions. Researchers have explored different types of Z-scheme materials and redox mediators to enhance photocatalytic performance. Traditional electron mediators have limitations, leading to the exploration of all-solid-state Z-scheme photocatalytic systems using solid conductors as electron mediators [13,14]. Direct Z-scheme photocatalytic systems, such as TiO₂/g-C₃N₄ [15] and WO₃/BiVO₄ [16], have also attracted considerable interest due to effective charge separation.

As a novel ternary oxide semiconductor material, BiOBr has drawn considerable attention in recent years for its special crystal structure composed of alternating Bi₂O₂ layers and Br layers [17]. In the Bi₂O₂ layer, bismuth ions exhibit a six-coordinated geometric configuration, while the Br layer is composed of bromine ions. This layered structure gives BiOBr a relatively large specific surface area, which is advantageous for the separation and migration of photogenerated electrons and holes, thereby facilitating photocatalytic degradation of organic pollutants or photocatalytic reduction of CO₂ [18]. Additionally, as versatile material, CeO₂ has garnered significant interest due to its unique properties [19]. One of the key features of CeO₂ as a photocatalyst is its

* Corresponding author.

E-mail address: xyli@dlut.edu.cn (X. Li).

<https://doi.org/10.1016/j.apcatb.2024.124248>

Received 1 April 2024; Received in revised form 24 May 2024; Accepted 26 May 2024

Available online 28 May 2024

0926-3373/© 2024 Elsevier B.V. All rights are reserved, including those for text and data mining, AI training, and similar technologies.

ability to generate and utilize oxygen vacancies, which play a crucial role in its photocatalytic activity [20,21]. These oxygen vacancies can act as active sites for adsorption and activation of reactant molecules, leading to enhanced catalytic performance [22]. In addition, CeO_2 has a cubic fluorite crystal structure, where each cerium ion is surrounded by eight oxygen ions. This structure gives CeO_2 unique oxygen storage and release capabilities, making it an excellent catalyst for various redox reactions [23,24].

Inspired by the aforementioned concepts and strategy, the combination of CeO_2 and BiOBr in the Z-type heterostructure would create synergistic effects that enhance the overall photocatalytic performance. CeO_2 provides oxygen vacancies and unique oxygen storage/release capabilities, while BiOBr offers a large specific surface area for effective separation and migration of charge carriers. As expected, the composite exhibits a remarkable photo-oxidation degradation ability for o-DCB and CO_2 reduction capability. The charge transfer dynamics of this direct Z-scheme was explored by surface photovoltage technique and time-resolved PL (TR-PL) spectra. X-ray photoelectron spectroscopy and density function theory (DFT) calculations were employed to confirm the Z-scheme structure in $\text{CeO}_2/\text{BiOBr}$ composite. The improved photo-oxidation degradation ability and CO_2 reduction performance of the heterostructure, in contrast to the individual CeO_2 and BiOBr components, suggest that this Z-schemes system efficiently facilitates the recombination, transfer and utilization of photogenerated charge carrier.

2. Experimental section

2.1. Materials

All chemical reagents which were purchased from Sino pharm Chemical Reagents Co., Ltd., China, were analytical grade and used without further purification.

2.2. Synthesis of materials

2.2.1. BiOBr microflower

BiOBr microflower was prepared according to our previously reported method [25]. In a typical synthesis, 1.5 mmol of KBr was added to 16 mL of absolute ethanol and then transferred to an ultrasonic cleaner for dispersion for 10 minutes. Following this, equimolar amount of $\text{Bi}(\text{NO}_3)_3 \cdot 5 \text{H}_2\text{O}$ was slowly introduced into the above dispersion with magnetic stirring for 2 hours at room temperature. Subsequently, the mixture was transferred into a 20 mL Teflon-lined stainless autoclave, sealed, and heated at 140°C for 12 hours under autogenous pressure. The system was then allowed to cool naturally to room temperature. The resulting precipitates were collected by centrifugation, washed with deionized water and ethanol several times. Finally, the obtained product was dried at 60°C in air for further characterization, and the resulting sample was designated as BiOBr MF.

2.2.2. Synthesis of CeO_2 nanoparticles

In a typical synthesis: First, 5.45 g of $\text{Ce}(\text{NO}_3)_3 \cdot 6 \text{H}_2\text{O}$ was dissolved in 50 mL of 80 % ethanol-water solution by volume. Then, the solution was vigorously stirred at 50°C until a homogeneous transparent solution was formed. Next, 12 mL of 3.0 M NH_4OH solution was slowly add to the above solution. The transparent solution will turn into a yellow suspension. Then, this suspension continue to be vigorously stirred at 50°C for 24 hours in an oil bath. Afterward, the resulting precipitate was collected by centrifugation, and washed several times with deionized water and anhydrous ethanol. The washed precipitate was dried in an 80°C oven for 24 hours. Finally, the dried sample was calcined at 500°C for 1 hour in a muffle furnace, with a heating rate of $1^\circ\text{C}/\text{min}$.

2.2.3. Synthesis of $\text{CeO}_2/\text{BiOBr}$ composite

First, 1.5 mmol of KBr was add to 16 mL of ethanol, and then

sonicated for 10 minutes, followed by vigorous stirring for 1 hour to form a micro-solution A. Then, an equilateral amount of $\text{Bi}(\text{NO}_3)_3 \cdot 5 \text{H}_2\text{O}$ was slowly added to the above solution, stirred at room temperature for 2 hours, and then 0.172 g of the as-prepared CeO_2 NP was added, and stirred vigorously for 1 hour. Next, this mixed suspension was poured into a 20 mL polytetrafluoroethylene reaction kettle and react at 140°C for 12 hours. After naturally cooling to room temperature, the resulting precipitate was collected by centrifugation, washed several times with deionized water and ethanol, and then dried it at 60°C to obtain the final product.

2.3. Characterization

The morphologies of the samples were observed using a field emission scanning electron microscope (FE-SEM, JEOL JSM-6360LV). The micro-structures of the catalysts were examined through transmission electron microscopy (TEM, JEOL JEM-2000 EX) and high-resolution transmission electron microscopy (HRTEM, FEI Tecnai G2 F30 microscope with an acceleration voltage of 300 kV). Powder X-ray diffraction (XRD) analysis was conducted using a Rigaku D/Max 2550VB/PC diffractometer with a $\text{Cu K}\alpha$ radiation source (1.5406 \AA). X-ray photoelectron spectroscopy (XPS) was performed on a Perkin-Elmer PHI 5600 electron spectrometer with $\text{Al K}\alpha$ radiation under ultrahigh vacuum conditions. The surface adventitious carbon (C 1 s) at 284.6 eV was used to calibrate the other binding energies. To detect the existence of oxygen defects, electron spin resonance (ESR) measurements were carried out on a Bruker (A200-9.5/12) at liquid nitrogen temperature, operating at the X band ($\sim 9.43 \text{ Hz}$). The magnetic field was modulated at 100 kHz, and the g value was determined from the precise frequency and magnetic field values.

The specific surface area and pore structures were examined through nitrogen adsorption-desorption isotherms at 77.3 K using an automated adsorption analyser (Quadasorb-SI) by the multipoint method. The optical properties of the samples were explored by a UV-vis spectrophotometer (JASCO, UV-550). The steady-state photoluminescence (PL) and time-resolved PL (TR-PL) spectra were examined by an FLSP-920 Edinburgh instrument with a 450 W xenon lamp monochromatized by double grating. The surface photovoltage (SPV) measurement was performed on a home-built apparatus, which consisted of a source of monochromatic light (model Omni- λ 3005), a photovoltaic cell, and a lock-in amplifier (SR830-DSP) with a light chopper (SR540) running at a frequency of 20 Hz. Transient-state surface photovoltage measurement was carried out with a self-assembled equipment in air atmosphere at room temperature, as previously reported by Wang and coworkers [35]. The laser radiation pulse (wavelength of 355 and pulse width of 5 ns) from a third-harmonic Nd: YAG laser (Polaris II, New Wave Research, Inc.) was used to excite the TPV. The signals were recorded by a 500 MHz digital phosphor oscilloscope (TDS 5054, Tektronix) with a preamplifier. ESR signals of the reactive oxide species were detected on a Bruker ECS106 X-Band spectrometer, with 5,5'-dimethyl-1-pyrroline-N-oxide (DMPO) as the trapping agent. Detailed experimental conditions included a temperature of 298 K, microwave power of 20 mW, center field of 3400 G, frequency of 9.865 GHz, and modulation amplitude of 1.00 G.

The electronic property of $\text{CeO}_2\text{-BiOBr}$ heterostructure and the charge transfers between them are investigated by the Vienna Ab-initio Simulation Package (VASP) using the Perdew-Burke-Ernzerhof (PBE) of the generalized gradient approximation (GGA). The PAW pseudo-potentials were used to calculate the interaction between valence electrons and the ionic core. Considering the lattice matching, $3 \times 2 \times \{111\}$ supercell and $3 \times 3 \times \{001\}$ supercell were used to simulate CeO_2 and BiOBr layers, respectively. A plane-wave basis with energy cutoff of 400 eV and an energy convergence of $1.0 \times 10^{-4} \text{ eV}$ at the gamma point are used to perform the geometry optimization. After geometry optimization, the energy convergence of $1.0 \times 10^{-5} \text{ eV}$ and the Monkhorst-Pack k-point mesh of $2 \times 2 \times 1$ are used to calculate the charge density

difference mapping between CeO_2 and BiOBr and their projected density of state (PDOS) plots.

2.4. In situ FTIR studies and photocatalytic activity evaluation

In situ FTIR spectra of the reactants on the $\text{CeO}_2/\text{BiOBr}$ composite were obtained using a FTIR spectrometer (Bruker VERTEX 70-FTIR) with a custom-made reaction apparatus, which is a quartz cell of approximately 160 mL volume, equipped with two KBr windows and a sample holder for placing the catalyst wafer (20 mg). All FTIR spectra were recorded by accumulating 64 scans at a resolution of 4 cm^{-1} . The photocatalytic activity of the prepared samples was measured under visible light illumination ($\lambda > 420\text{ nm}$) emitted by a Xenon lamp (XQ-500 W) with a 420 nm UV-cutoff filter. In a typical test, the pressed wafer was placed in the sample holder, and the reaction cell was sealed with air at a relative humidity of about 45 %. A small quantity of o-DCB (3 μL) was then injected into the reaction equipment from the rubber tube. After approximately two hours in the dark, the fully volatilized o-

DCB reached adsorption equilibrium. Subsequently, the Xenon lamp was turned on, initiating the photocatalytic reaction. The concentrations of o-DCB in the reaction process were detected using an off-line gas chromatogram (Agilent 7890 A) equipped with FID (HP-5 capillary column) and TCD (Porapak Q).

CEL-SPH2N photocatalysis was used to evaluate the CO_2 reduction system. 0.05 g of the photocatalyst was dispersed in the mixed solution containing 90 mL of deionized water, and put in a closed quartz reactor. A 300 W Xe lamp equipped with a cutoff filter of 420 nm was used to provide visible light irradiation ($\lambda > 420\text{ nm}$). Before reaction, the reaction system was evacuated to ensure complete removal of air, CO_2 gases in the solution by aeration of Ar. It was maintained at $25\text{ }^\circ\text{C}$ by a water constant temperature system. Then the light was left on for 6 hours to catalyse the CO_2 reduction reaction. (Shanghai Fan Wei Science and Technology Ltd. GC 9860, 5 A column, TCD, and Ar carrier).

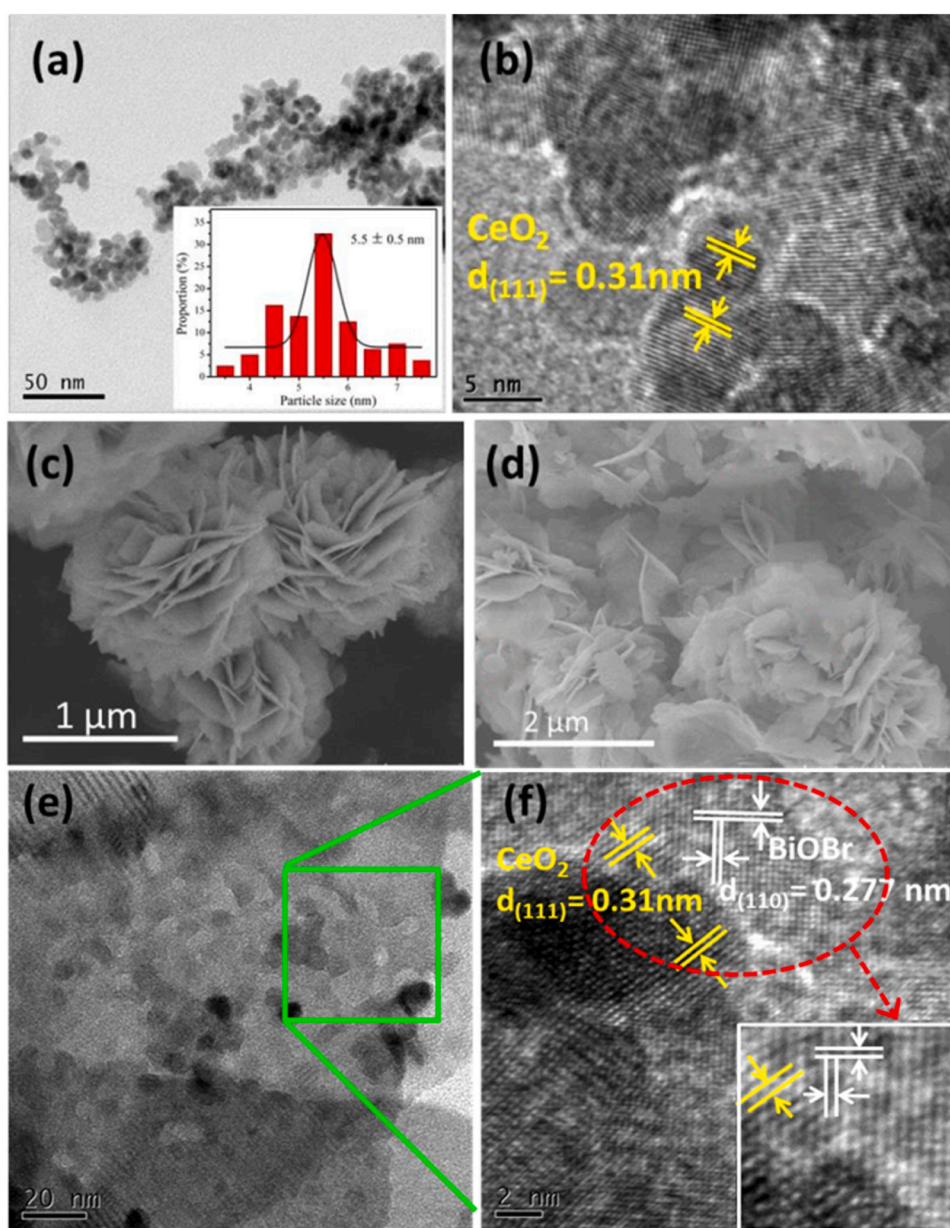


Fig. 1. Typical TEM and HRTEM images (a, b) of CeO_2 nanoparticles, SEM images of BiOBr microflowers (c) and $\text{CeO}_2/\text{BiOBr}$ composite (d), and typical HRTEM images (e, f) of $\text{CeO}_2/\text{BiOBr}$ composite.

3. Results and discussion

To accurately illustrate the morphologies and microstructures of pure CeO₂, BiOBr and CeO₂/BiOBr composite, SEM, TEM and HRTEM analyses were conducted. As displayed in Fig. 1a, the morphology of the as-prepared CeO₂ sample can be observed to be uniform nanoparticles with the grain diameter of 5.5 nm statistically. In Fig. 1b, a typical HRTEM image of the CeO₂ nanoparticles shows clear lattice fringes with lattice spacing of 0.31 nm, assigned to (111) atomic planes of CeO₂, which is indication of its high crystallinity. In addition, the morphology and microstructure of the as-prepared BiOBr sample was analyzed detailedly in our previous work [25]. As shown in Fig. 1c and Fig. S1a, the flower-like BiOBr is loosely assembled by stacking ultrathin nanoflakes with length about 600 nm, constructing the hierarchical architecture with a large amount of open-free space, which can provide the large contact area for reactants. Fig. 1d illustrates the morphology of the CeO₂/BiOBr composite, in which CeO₂ nanoparticles are loaded onto the surface of the BiOBr microflowers. To obtain a more detailed visualization of the CeO₂ nanoparticles, which are relatively small in size, TEM characterization was performed. In Fig. 1e, it can be seen that the CeO₂ nanoparticles have been uniformly anchored on the surfaces of the assembly unites of BiOBr microflower. Furthermore, the HRTEM image (Fig. 1f) of the area marked by the green square in Fig. 1e provides a closer examination of the crystal structures. The observed lattice fringe spacings of 0.310 and 0.277 nm were attributed to the (111) plane of CeO₂ and the (110) plane of BiOBr, respectively, revealing that CeO₂ nanoparticles were intimately combined with the BiOBr microflowers, and the heterojunction microstructure in the interface was constructed.

Fig. 2 displays the XRD patterns of the as-prepared CeO₂ nanoparticles, BiOBr microflowers and CeO₂/BiOBr composite. In Fig. 2, the XRD patterns of CeO₂ match well with body-centered cubic CeO₂ (JCPDS no. 34-0394) and the diffraction peaks located at 2θ of 28.65°, 33.12°, 47.65° and 56.4° could be indexed to the (111), (200), (220) and (311) crystal planes of cubic CeO₂, respectively. On the basis of the Scherrer equation [26], the crystallite size of CeO₂ is calculated to be 6.0 nm from the intensity of diffraction peak over the prominent the (111) crystal plane, almost in consistence with the statistical size. In addition, the XRD patterns of the BiOBr microflowers can correspond to the tetragonal phase of BiOBr (JCPDS No. 73-2061). In the two XRD patterns, no other phases are detected, suggesting that the as-prepared samples are pure in crystalline phase. For the CeO₂/BiOBr sample, the XRD patterns exhibit a combination of the two diffraction sets of CeO₂ (marked by ♦ and ▽) and BiOBr, indicating the formation of CeO₂/BiOBr composite. Due to the low content of CeO₂, the diffraction peaks display relatively weaker intensity compared to those of BiOBr microflowers.

The XPS spectra were employed to detect surface elemental

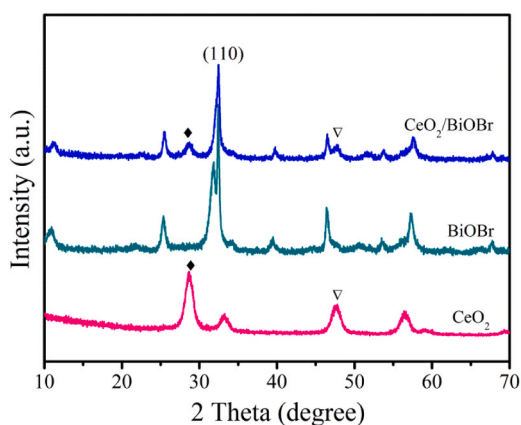


Fig. 2. XRD patterns of pure CeO₂ nanoparticles, pure BiOBr microflowers and the CeO₂/BiOBr composite.

compositions, valence states and chemical environment over the materials. As displayed in Fig. 3a, the survey XPS spectrum of CeO₂/BiOBr composite confirms that the material is composed of Bi, Br, O and Ce elements, indicating that CeO₂ is successfully combined with BiOBr. Besides, the observed C 1 s peak around 284.6 eV is attributed to the adventitious carbon in instrument used for calibration. Additionally, the high resolution XPS spectra of Bi 4 f, Ce 3d and O 1 s are exhibited in Fig. 3b-d. In Fig. 3b, the observed peaks at around 159.0 eV and 164.3 eV can be ascribed to Bi 4 f_{7/2} and Bi 4 f_{5/2}, respectively, confirming that the bismuth specie in the sample is Bi³⁺ [27]. As shown in Fig. 3c, the XPS Ce 3d spectra of CeO₂ nanoparticles and CeO₂/BiOBr composite can be fitted into eight peaks [28]. Among them, the two peaks labeled as u' and v' are assigned to the existence of Ce³⁺, while other bands are the signatures of Ce⁴⁺. The peaks labeled as u, u'' and u''' arise from Ce⁴⁺ 3d_{3/2}, and the peaks labeled as v, v'' and v''' correspond to Ce⁴⁺ 3d_{5/2}. Thus, the multiple peaks in the Ce 3d are attributed to a mixture of the Ce³⁺ and Ce⁴⁺ oxidation states, in which the Ce³⁺ is mainly derived from the formation of oxygen vacancies [29]. The relative surface ratios of Ce³⁺/Ce⁴⁺ in CeO₂ nanoparticles and CeO₂/BiOBr composite are calculated to be ca. 19.4 % and 25.4 %, respectively, according to the following equations by the corresponding peak areas (denoted as Ce (III) and Ce (IV)).

$$\text{Ce (III)} = v' + u' \quad (3.1)$$

$$\text{Ce (IV)} = v + v'' + v''' + u + u'' + u''' \quad (3.2)$$

$$[\text{Ce (III)}] = \text{Ce (III)} / [\text{Ce (III)} + \text{Ce (IV)}] \quad (3.3)$$

It is reported that the higher Ce³⁺ ratio is beneficial for the adsorption of oxygen species and the activation of reactants [30]. The XPS spectra of O 1 s region are displayed in Fig. 3d. For BiOBr microflowers and CeO₂ nanoparticles, the asymmetrical O 1 s signals are fitted into two sets of sub-bands denoted as O_α (O_α') and O_β (O_β'), respectively. The O_α (529.9 eV) and O_β (528.9 eV) peaks correspond to the lattice oxygen in BiOBr and CeO₂, respectively [31], and the bands labeled as O_α' (531.2 eV) and O_β' (530.9 eV) are assigned to surface adsorbed oxygen (e.g. oxygen in hydroxyl-like groups or H₂O) [32]. However, for the CeO₂/BiOBr composite, the O 1 s peaks can be fitted into three sub-bands denoted O_β'', O_α'' and O_γ, which are attributed to the Ce–O and Bi–O bands, and surface adsorbed oxygen, respectively. Besides, the sub-bands of the CeO₂/BiOBr composite have obvious shift to higher binding energies compared with the pure BiOBr and CeO₂ samples, implying that the chemical environment of elements have been changed, due to charge redistribution caused by the compounding between CeO₂ nanoparticles and BiOBr microflowers.

To elucidate coordination geometry of cerium ion as well as its valence states, and confirm the existence of oxygen vacancies, low-temperature ESR spectra have been carried out. As shown in Fig. 4, for the pure CeO₂, a sharply isotropic signal at about

$g_{\perp} = 1.967$ with axial symmetry is observed, which is reportedly assigned to Ce³⁺ ions formed within calcination under air [33–35], and the isotropic signal at $g = 1.976$ is attributed to the unpaired electrons trapped in defects or localized in anion vacancies [36]. Besides, the anisotropic signals at about $g = 2.033$ and 2.039 are respectively attributed to adsorbed O₂⁻ species, and the paramagnetic species of Ce⁴⁺–O₂⁻, which is mainly derived from coordinative unsaturation of Ce³⁺ upon oxygen adsorption [37]. However, compared to pure CeO₂ nanoparticles, the intensities of these ESR signals over CeO₂/BiOBr composite are weaker, mainly due to the low CeO₂ nanoparticles loading on BiOBr microflowers. In addition, it is worth noting that the signal at $g = 2.001$ can be unambiguously observed in the ESR spectrum of CeO₂/BiOBr composite, which is belonged to the paramagnetic species resulted from oxygen vacancies trapping and stabilizing single electrons. Therefore, ESR results suggest that Ce³⁺ ions and oxygen vacancies both existed in CeO₂/BiOBr composite, which can facilitate the separation and transferring of the charge carries.

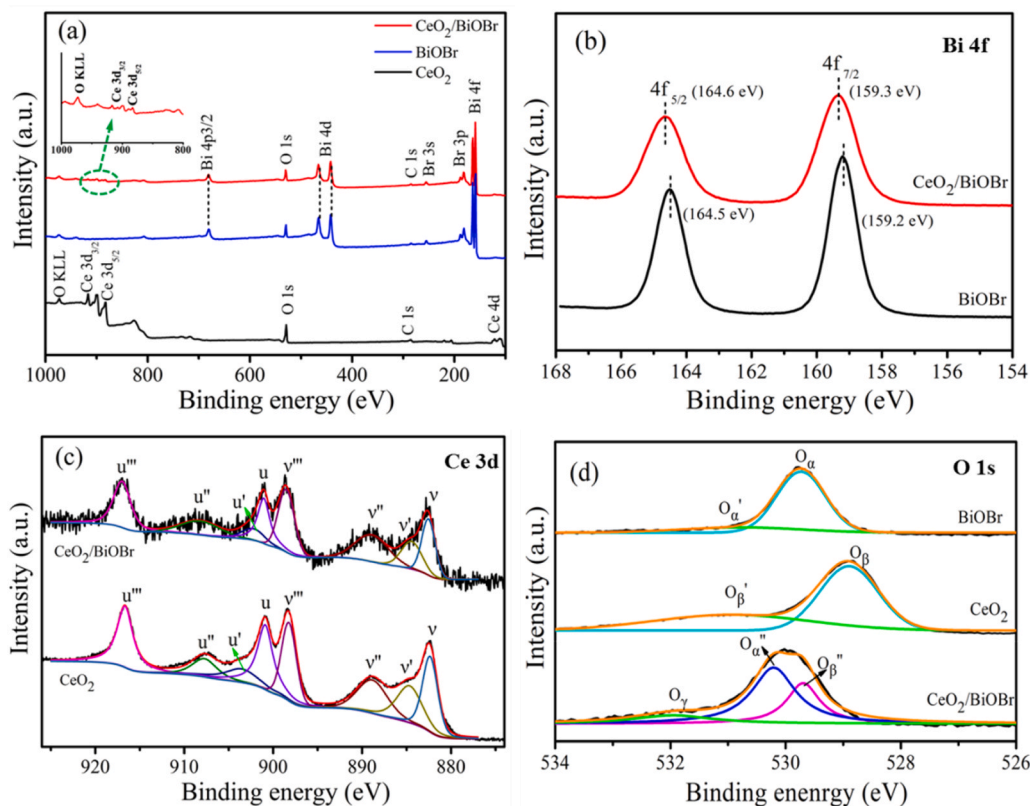


Fig. 3. XPS spectra of CeO_2 , BiOBr and $\text{CeO}_2/\text{BiOBr}$ catalyst. Survey (a) and high-resolution XPS spectra of $\text{Bi } 4f$ (b), $\text{Ce } 3d$ (c) and $\text{O } 1s$ (d).

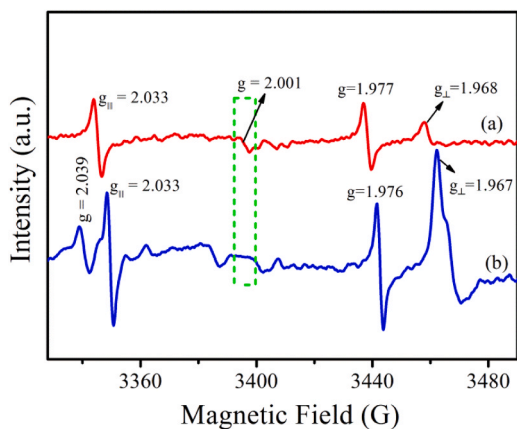


Fig. 4. ESR spectra of $\text{CeO}_2/\text{BiOBr}$ composite (a) and CeO_2 nanoparticles (b) measured at $T=100$ K.

The pore structure characteristics of the obtained samples were explored through nitrogen sorption isotherms (inset) and pore size distribution curves as shown in Fig. 5. All of the as-prepared catalysts exhibit type-IV adsorption-desorption isotherm with a H1 hysteresis loop, indicating the existence of mesopore structure [27,38]. The narrow pore size distributions are observed for CeO_2 nanoparticles and $\text{CeO}_2/\text{BiOBr}$ composite, suggesting that their pore sizes are comparatively uniform. In addition, the detailed BJH pore size distribution and Brunauer–Emmett–Teller (BET) specific surface area are summarized in Table S1. The specific surface areas of CeO_2 nanoparticles, BiOBr microflowers and $\text{CeO}_2/\text{BiOBr}$ composite are $100 \text{ m}^2 \text{ g}^{-1}$, $24 \text{ m}^2 \text{ g}^{-1}$ and $29 \text{ m}^2 \text{ g}^{-1}$, respectively. Compared with pure BiOBr microflowers, the specific surface area of the $\text{CeO}_2/\text{BiOBr}$ composite was slightly increased after small amount of CeO_2 nanoparticles loading.

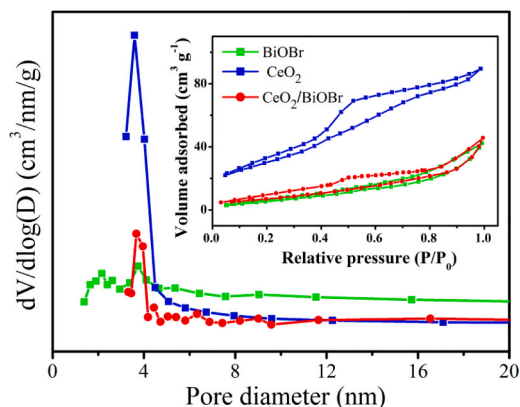


Fig. 5. BJH pore size distribution curves of the BiOBr microflowers, CeO_2 nanoparticles and $\text{CeO}_2/\text{BiOBr}$ composite and the corresponding N_2 adsorption-desorption isotherms (inset).

In order to investigate the optical absorption properties of the as-prepared samples, the UV-Vis diffusion spectroscopy has been carried out. As displayed in Fig. 6a, the synthesized samples all exhibit favorable light absorption ability in the wavelength less than 450 nm. Comparing with the CeO_2 nanoparticles, the $\text{CeO}_2/\text{BiOBr}$ composite possesses superior visible-light absorption ability, whose absorption edge is at around 500 nm. Additionally, the optical band gap energies have been estimated from the Tauc's plots by the equation $(\alpha h\nu) = A(h\nu - E_g)^{n/2}$, where α , h , A , ν and E_g are the optical absorption coefficient, Planck constant, proportionality constant, light frequency and band gap energy, respectively, and the value of exponent is determined by the electronic transition property of the material, such as $n = 1$ for direct transition, and $n = 4$ for indirect transition [39,40]. In the present study, E_g of the CeO_2 and BiOBr is deduced from the plots of $(\alpha h\nu)^2$ versus $h\nu$, and

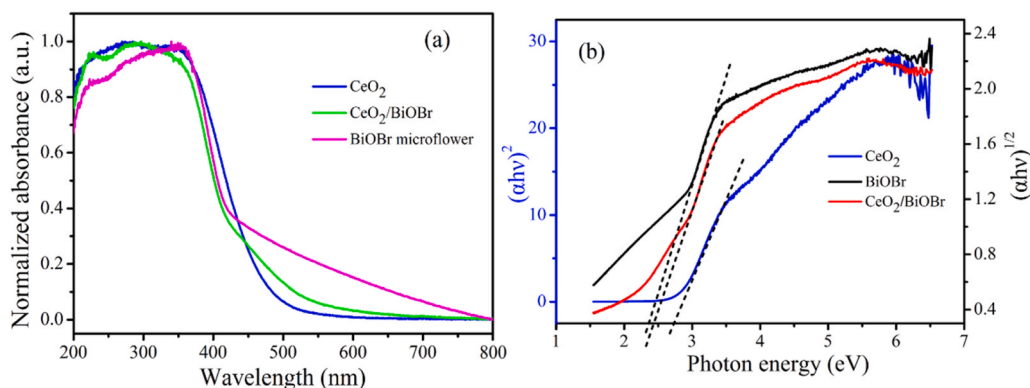


Fig. 6. Normalized UV-vis diffuse reflectance spectra (a) and Tauc plots (b) of CeO₂ nanoparticles, BiOBr microflowers and CeO₂/BiOBr composite.

$(\alpha h\nu)^{1/2}$ versus $h\nu$, respectively. As shown in Fig. 6b, the estimated band gap values of BiOBr microflowers, CeO₂ nanoparticles and CeO₂/BiOBr composite are 2.39, 2.74 and 2.45 eV, respectively.

PL emission spectrum is closely associated with the recombination of excited electrons and holes. Generally, weaker PL emission intensity usually indicates lower density of recombination centers and higher separation efficiency of electron-hole pairs. Fig. 7a displays the PL excitation spectra of the materials, as can be seen from which the strongest photoluminescence peak is located at 331 nm for CeO₂ nanoparticles and CeO₂/BiOBr composite. The strongest photoluminescence peak appears at 384 nm for BiOBr microflowers. Thus, 384 nm and 331 nm are used as the excitation wavelength for BiOBr microflowers, CeO₂ nanoparticles and the CeO₂/BiOBr composite, respectively. When the material is irradiated by the specific excitation wavelength, the electrons in the valance band (VB) are excited to the conduction band (CB), and then the excited electrons with different energy levels in the CB can be relaxed through different recombination processes, thus, resulting in a luminescence emission [41].

Fig. 7b presents the corresponding emission spectra of the as-prepared samples. Obviously, it can be seen that the CeO₂/BiOBr composite exhibited a similar emission spectrum as CeO₂ nanoparticles, while was different from that of BiOBr microflowers. For BiOBr microflowers, the specific explanation on its emission spectrum can be observed in our previous work [25]. In the PL emission spectrum of CeO₂ nanoparticles, the excitonic PL signal such as the strong blue emission at about 480 nm and yellow emission at 620 nm, may be ascribed to the electron transition from the energy traps induced by surface oxygen vacancies or defects in the O 2p valence band of the CeO₂ nanoparticles [42]. Compared with the pristine CeO₂ and BiOBr materials, the CeO₂/BiOBr composite shows notably diminished PL intensity, implying that the radiative recombination of the photoinduced exciton is suppressed effectively and the separation of charge carriers over CeO₂/BiOBr composite is promoted positively.

To further elucidate the interfacial charge transfer dynamics of the CeO₂/BiOBr composite, time-resolved PL spectroscopy which can provide important information about the exciton lifetime was carried out.

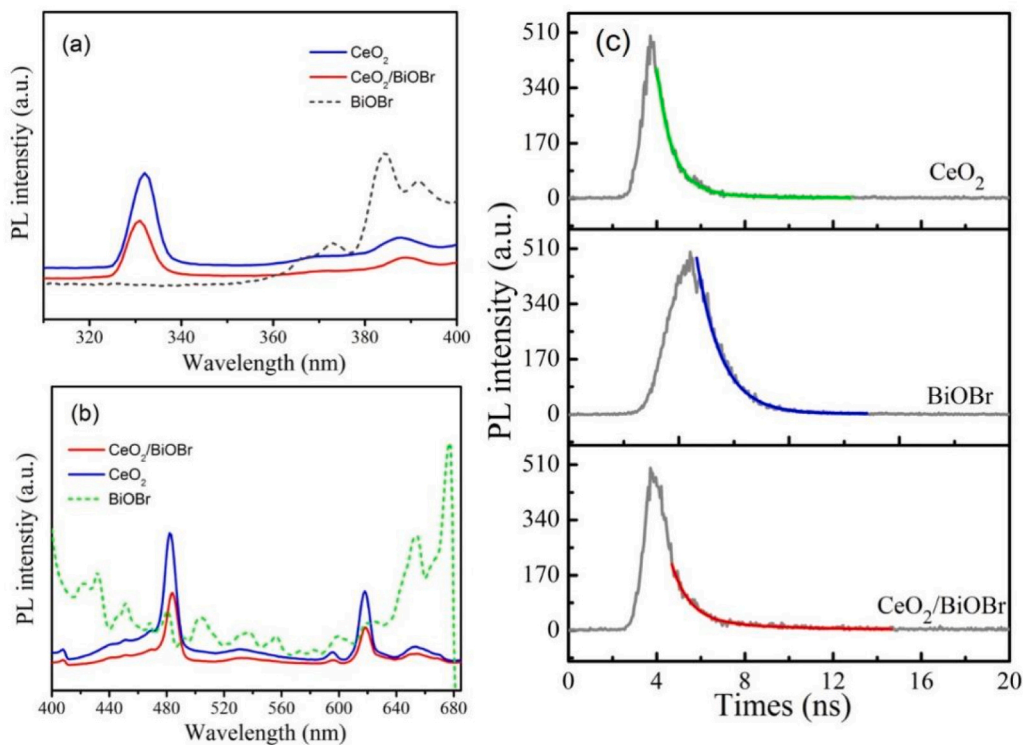


Fig. 7. PL spectra of the as-prepared samples: (a) excitation spectra, (b) emission spectra with excitation wavelength at 331 nm and 384 nm, respectively, (c)TRPL spectra of the samples and the corresponding fit curves.

The measurement results are displayed in Fig. 7c, and the fitted lifetimes of the PL decay profile are summarized in Table 1. As shown in Fig. 7c, the PL peak decay of CeO₂/BiOBr composite was obviously slower than those of the pure CeO₂ nanoparticles and BiOBr microflowes, indicating efficient charge transfer in the interface of CeO₂/BiOBr composite. In addition, it can be observed from Table 1 that BiOBr microflowes exhibited single-exponential decay, while CeO₂/BiOBr composite and CeO₂ nanoparticles exhibited biexponential decay. In the biexponential decay function $I(t) = B_1 \exp(-t/\tau_1) + B_2 \exp(-t/\tau_2)$, $I(t)$ is the PL intensity, τ_1 and τ_2 are the decay times, and B_1 and B_2 are the relative corresponding magnitudes [43]. Generally, the biexponential model suggested that two emissive states were involved in the PL decay with a fast decay constant (τ_1) and a slow constant (τ_2), which are originated from radiative emissions via direct band-band exciton recombination and indirect recombination of trapped electrons with VB holes, respectively [44,45].

As shown in Table 1, direct inter-band exciton recombination was predominated in the pure BiOBr microflowes, which is revealed by the high proportion of short-living component ($B_1\tau_1$, 100 %), and both direct recombination and indirect recombination of excitons existed in pure CeO₂ nanoparticles and CeO₂/BiOBr composite. Furthermore, the τ_1 value and τ_2 value of CeO₂/BiOBr composite are longer than that of CeO₂ nanoparticles, and the proportion of the long-living component ($B_2\tau_2$, 46.43 %) is higher than that of pure CeO₂ nanoparticles ($B_2\tau_2$, 25.41 %), indicating that the lifetime of photo-generated charge carriers was prolonged and more efficient trapping of electrons on the defect states occurred in CeO₂/BiOBr composite, eventually resulting in the efficient separation and transfer of the charge carriers.

As an efficient tool for exploring localized charge separation at surfaces or interfaces of photocatalysts, the SPV measurement technique has been carried out in this work. Typical ac SPV spectra obtained on a lock-in amplifier for the as-prepared samples are shown in Fig. 8a. Generally, a stronger intensity of SPV response indicates a higher charge separation efficiency. From Fig. 8a, it can be seen that the SPV response of the CeO₂/BiOBr composite is significantly stronger than that of pure BiOBr microflowes and pure CeO₂ nanoparticles. The SPV amplitude of CeO₂/BiOBr composite at approximately 350 nm is as high as 175 μ V, which is about 1.7 times of that of BiOBr microflowes (103 μ V). For pure CeO₂ nanoparticles, the SPV response is greatly weak and the amplitude is less than 4 μ V (inset). The result suggests that the separation of excess holes and electrons in CeO₂/BiOBr composite is more efficient, which could be derived from the construction of built-in electric field between CeO₂ nanoparticles and BiOBr microflowes.

To study the dynamics of photo-generated charge carriers, the transient photovoltage (TPV) technique is employed because it can provide direct evidences on the photo-induced charge carriers generation, lifetime and separation, as well as charge transport direction. As shown in Fig. 8b, for pure CeO₂ nanoparticles, the weak signal took a relatively long time to reach its maximum. However, the TPV signal of CeO₂/BiOBr composite have basically no retardation and directly reached the maximum, implying that CeO₂/BiOBr composite has superior charge carrier mobility performance. Additionally, it can be found that the TPV responses of CeO₂/BiOBr composite and pure BiOBr microflowes are positive under laser pulse irradiation with 355 nm, indicating the photoinduced holes accumulation at the surface area nearby the testing electrode [46]. The positive TPV responses of BiOBr

microflowes and CeO₂/BiOBr composite could be divided into two components: one fast ($< 10^{-7}$ s) and one slow ($> 10^{-4}$ s). Generally, the fast component is mainly corresponding to the separation of photoinduced charges under the impact of built-in electric field. As a n-type semiconductor, the built-in electric field direction of BiOBr microflowes is from the inner to the outer, resulting in the accumulation of holes at the surface. The positive slow one mainly results from photo-induced holes diffusion to the surfaces because of the adsorbate capturing photoinduced electrons. Noticeably, the lifetime of photo-generated charge carries of BiOBr microflowes and CeO₂/BiOBr composite is much longer than that of pure CeO₂ nanoparticles, and the TPV response of CeO₂/BiOBr composite is strongest among the three components. It is assumed that the formation of specific heterojunction between BiOBr microflowes and CeO₂ nanoparticles, resulting in high separation and long lifetime of charge carriers for CeO₂/BiOBr composite.

To explore the photocatalytic activity of the as-prepared catalysts, o-DCB which has been frequently used as the precursor of persistent and highly toxic polychlorinated dibenzodioxins and dibenzofurans was employed as the target pollutant. As shown in Fig. 9a, through a blank experiment (without a catalyst), it can be seen that o-DCB was hardly degraded under direct exposure to visible light. The degradation ratio of o-DCB over the BiOBr microflowes and CeO₂ nanoparticles reaches about 68 % and 49 % after being treated for 6 h under visible-light irradiation, respectively. Furthermore, the degradation ratio of o-DCB over the CeO₂/BiOBr composite reaches as high as 78 % under the same condition. In order to quantitatively explicit the reaction kinetics of catalytic degradation of o-DCB over the samples, the experimental data was fitted through a pseudo-first-order rate law, and the corresponding kinetic constants were displayed in Fig. 9b. Obviously, the value of apparent rate constant over the CeO₂/BiOBr composite ($2.68 \times 10^{-1} \text{ h}^{-1}$) was the highest, which was about 1.18 and 2.23 times of that over the pure BiOBr microflowes and CeO₂ nanoparticles, respectively, confirming that the photodegradation performance of o-DCB over the CeO₂/BiOBr composite is the strongest. Besides, in situ FTIR spectroscopy was performed to investigate the evolution of adsorbed species, such as transient intermediates and final products, during the photo-oxidation process of o-DCB, which was displayed in Fig. S3.

The photocatalytic activity of the as-prepared BiOBr microflowes, CeO₂ nanoparticles, and CeO₂/BiOBr composite was further explored by reduction of CO₂ under visible-light irradiation. As displayed in Fig. 10, the yield rate of CO and CH₄ over pure BiOBr microflower was 50.97 $\mu\text{mol g}^{-1} \text{ h}^{-1}$ and 8.299 $\mu\text{mol g}^{-1} \text{ h}^{-1}$, while because of trace concentration of CO and CH₄, they were not detected over CeO₂ nanoparticles. However, after compounding the two catalysts, the yield of CO and CH₄ over CeO₂/BiOBr composites greatly increased, reaching as high as 64.27 $\mu\text{mol g}^{-1} \text{ h}^{-1}$ and 11.93 $\mu\text{mol g}^{-1} \text{ h}^{-1}$, which is 1.3 and 1.4 times of that over the pure BiOBr microflower. Thus, CeO₂/BiOBr composites show enhanced photocatalytic reduction activity of CO₂ in comparison with pure BiOBr microflowes, signifying the positive effect of CeO₂ nanoparticles loading, mainly attributed to the formation of an efficient heterojunction interface and the synergistic effects arising from the oxygen vacancies in CeO₂, which improve charge separation, CO₂ adsorption and activation, ultimately leading to superior photocatalytic performance.

The ESR-spin-trap technique (with DMPO as a trapping reagent) was employed to detect the reactive oxygen species (ROS) generated in the as-prepared catalysts irradiated with visible light ($\lambda > 420 \text{ nm}$). As displayed in Fig. 11a, the characteristic sextet ESR signal is assigned to DMPO- $\bullet\text{O}_2^-$ adducts. Obviously, the intensity of DMPO- $\bullet\text{O}_2^-$ adduct for CeO₂/BiOBr composite was much stronger than that for pure BiOBr microflowes and pure CeO₂ nanoparticles, implying that the photoelectrons transferred to the surface could be easily captured by molecular oxygen charged by the localized electrons of surface oxygen vacancies, ultimately forming $\bullet\text{O}_2^-$ radical [47,48]. In Fig. 11b, the typical four peaks are attributed to DMPO- $\bullet\text{OH}$ adduct. As same as EPR signal

Table 1
Photo-induced charge lifetimes and relative intensities of the as-synthesized samples.

Sample	B_1 (%)	τ_1 (ns)	B_2 (%)	τ_2 (ns)
BiOBr microflowes	100	1.125	–	–
CeO ₂ nanoparticles	74.59 %	0.671	25.41 %	1.731
CeO ₂ /BiOBr composite	53.57 %	0.803	46.43 %	3.701

Fit equation: $A + B_1 \exp(-t/\tau_1) + B_2 \exp(-t/\tau_2)$.

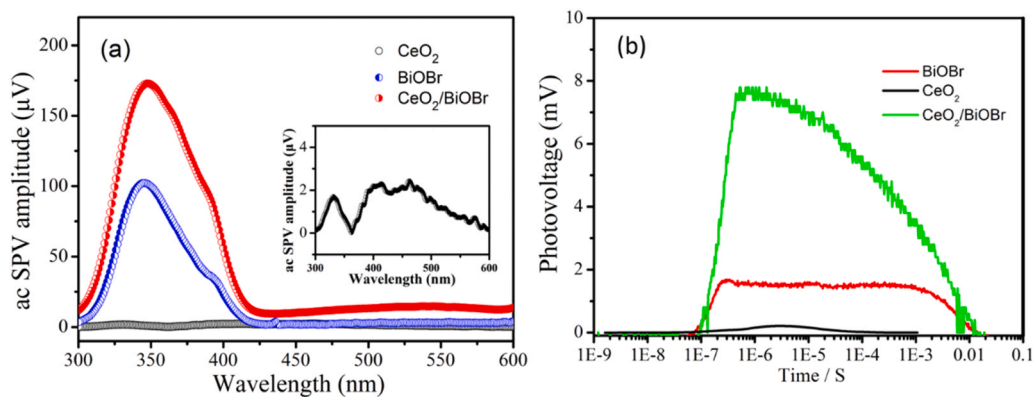


Fig. 8. SPV spectra (a) of the as-prepared catalysts and TPV responses (b) excited by the laser pulse at 355 nm.

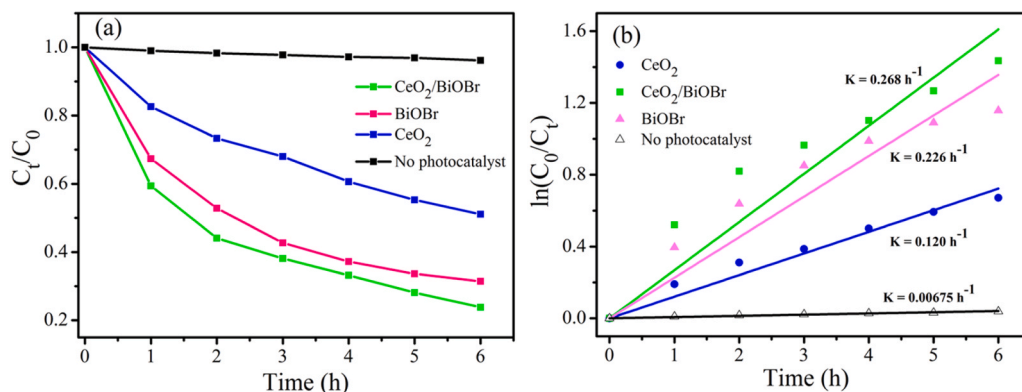


Fig. 9. Photocatalytic degradation rates (a) of o-DCB over the catalysts under visible-light irradiation ($\lambda > 420 \text{ nm}$) and (b) the corresponding pseudo-first-order kinetic fit curves.

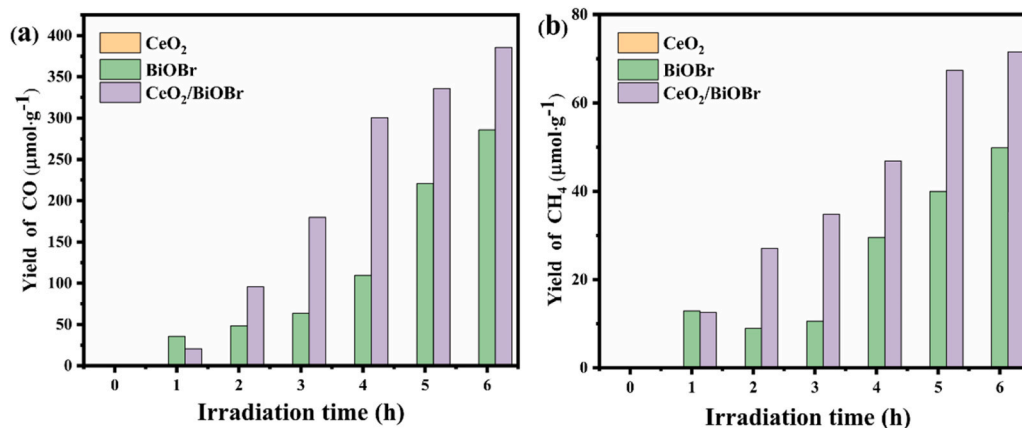


Fig. 10. Photocatalytic reduction CO₂ activity of CeO₂ nanoparticles, BiOBr microflowers, and CeO₂/BiOBr composite under visible-light irradiation ($\lambda > 420 \text{ nm}$).

of DMPO- $\bullet\text{O}_2^-$ adducts, the intensity of DMPO- $\bullet\text{OH}$ adduct for CeO₂/BiOBr composite are greatly stronger than that for pure BiOBr microflowers and pure CeO₂ nanoparticles, suggesting that the formed heterointerface of CeO₂/BiOBr composite is beneficial to the \cdot -transfer and utilization of the photoinduced carriers.

The structure simulation shows that the CeO₂-BiOBr composite interface consists of Bi-O bonds. The obtained charge density difference between CeO₂ and BiOBr layers indicates that the electrons (yellow region) tend to be transferred from BiOBr layer to CeO₂ layer (Fig. 12a). Besides, the averaged potential variation along the direction perpendicular to the CeO₂-BiOBr heterointerface shows that the Bi atoms of

BiOBr layer are located in a more positive regions than the Ce atoms of CeO₂ layer, which can also contribute the flowing of electron from BiOBr layer to CeO₂ layer (Fig. 12b). The results are consistent with the peak shift to the aspect of high binding energy in high-resolution XPS spectra of Bi 4f, in which a positive binding energy shift occurred, indicating a decrease of the electron density. In Fig. 12c, the PDOS plots further suggest that the conduction band edge potential of CeO₂ layer is more positive than that of BiOBr. In contrast, the valence band edge potential of CeO₂ layer is less negative than that of BiOBr. Combining with the experimental results, a Z-scheme photocatalytic mechanism is considered between BiOBr and CeO₂ in which BiOBr and CeO₂ act as PS I and

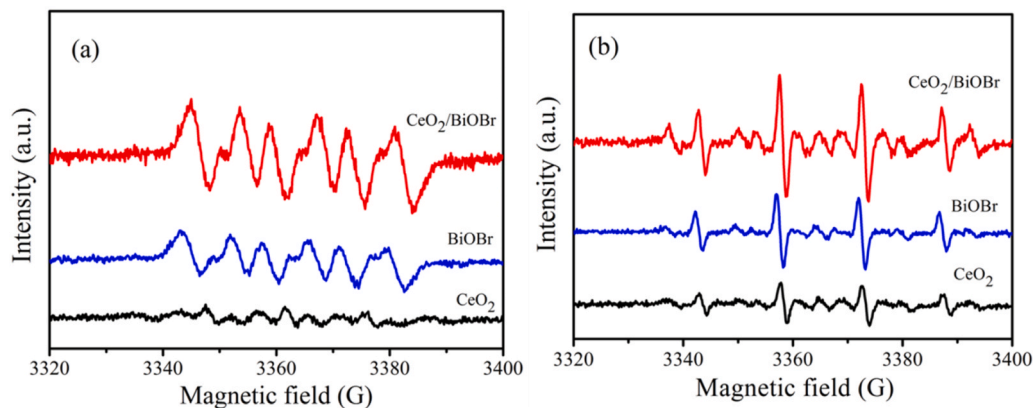


Fig. 11. ESR spectra of (a) DMPO- $\bullet\text{O}_2^-$ and DMPO- $\bullet\text{OH}$ (b) generated over the as-prepared samples.

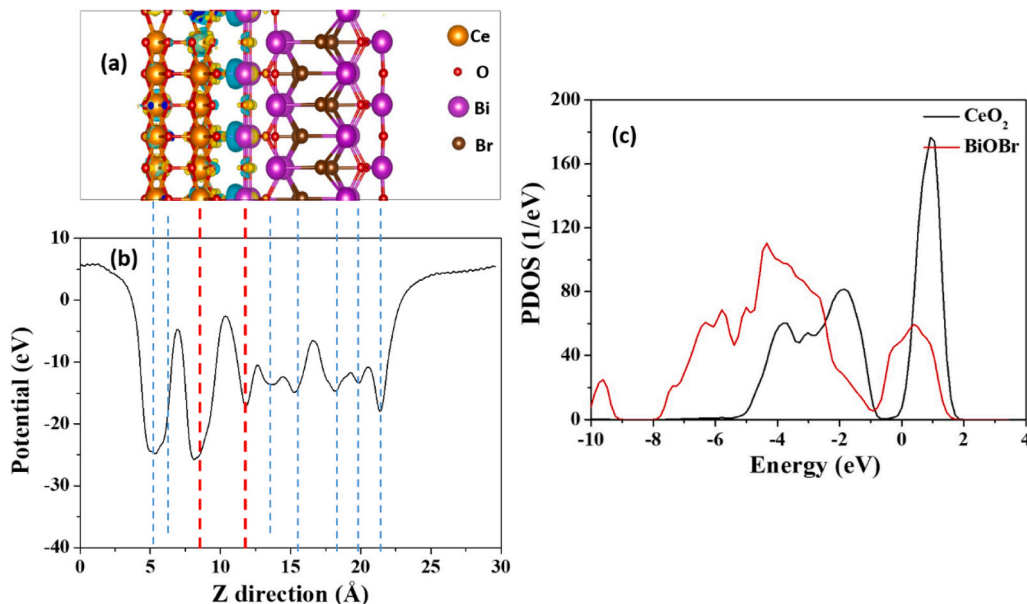


Fig. 12. (a) The charge density difference between CeO_2 and BiOBr layers. (b) The averaged potential variation along the direction perpendicular to the CeO_2 and BiOBr heterointerface. The isosurface of charge density is $0.005 \text{ e } \text{\AA}^{-3}$ for all figures. The yellow and skyblue isosurfaces stand for the negative charge and positive charge, respectively. (c) The projected density of state (PDOS) plots of CeO_2 and BiOBr layers.

PS II, respectively.

According to the above content, a profound analysis of the charge transfer mechanism of the Z-scheme heterojunction formed between CeO_2 nanoparticles and BiOBr microflowers is obtained. Structural simulations of CeO_2 and BiOBr indicate the presence of Bi-O bonds at their interface, providing a pathway for electron transfer. Additionally, electrostatic potential distribution calculations were employed to determine the energy barrier between BiOBr microflowers and CeO_2 nanoparticles. In this work, the main exposure facets of the BiOBr microflowers and CeO_2 nanoparticles are (001) facet and (111) facets, the crystal structures of which are displayed in Fig. 13a and b, respectively. As shown in Fig. 13 c and d, the work functions of BiOBr microflowers and CeO_2 nanoparticles (relative to the vacuum level) are 6.94 and 3.21 eV, respectively. According to the following relational calculation formula between E_F (vs NHE) and E_F (vs vacuum level) [49,50]

$$E_F \text{ (vs NHE, pH 0)} = -4.5 \text{ V} - E_F \text{ (vs vacuum level)} \quad (1)$$

and the Nernst equation:

$$E_F \text{ (vs NHE, pH 7)} = E_F \text{ (vs NHE, pH 0)} - 0.059 \text{ pH} \quad (2)$$

the E_F (vs NHE, pH 7) of BiOBr (001) and CeO_2 (111) at pH=7 relative to NHE are determined to be 2.03 and -1.70 eV, respectively. The Fermi level position of BiOBr (001) is much higher than that of CeO_2 (111). When CeO_2 nanoparticles and BiOBr microflowers contact intimately, the electrons spontaneously transfer from BiOBr to CeO_2 in order to equalize the Fermi levels, leading to the formation of an internal built-in electric field with the direction from BiOBr to CeO_2 . Furthermore, in order to achieve thermodynamic equilibrium, conduction band minimum (CBM) and valence band maximum (VBM) of BiOBr bend upwards, while the CBM and VBM of CeO_2 bend downwards.

This band bending creates an energy barrier for charge carrier transfer across the interface. Facilitated by the internal electric field and to overcome the smaller energy barrier, the photoexcited electrons in the CB of CeO_2 are injected into the VB of BiOBr . Based on the theoretical calculations and experimental results, we propose a Z-type charge transfer and separation mechanism as illustrated in the Fig. 13e, where BiOBr and CeO_2 act as PS I and PS II, respectively. In summary, the migration of charges in the Z-type heterojunction promotes the effective separation and utilization of photogenerated electrons and holes, thereby enhancing the photocatalytic redox performance.

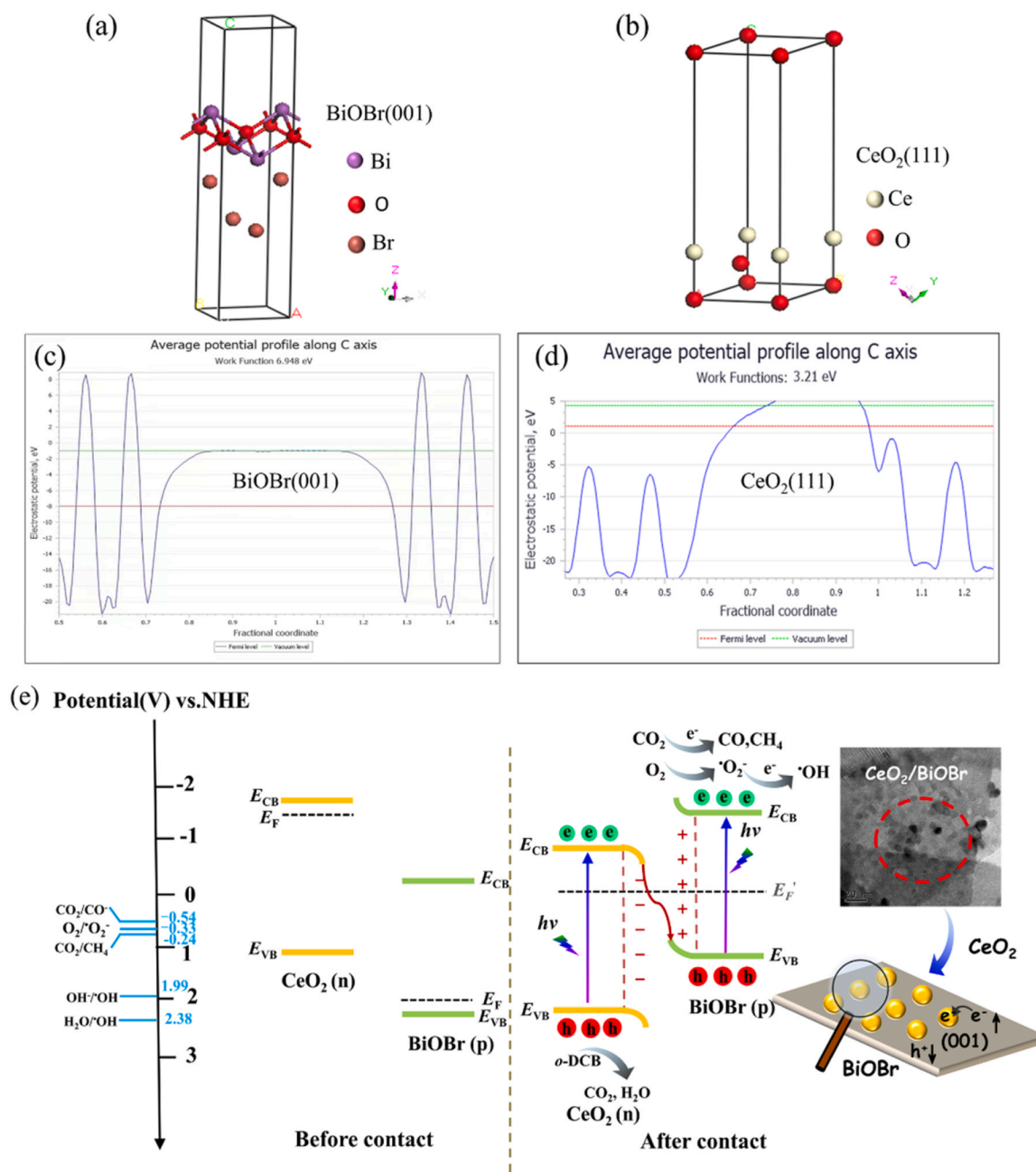


Fig. 13. (a, b) Crystal structures of BiOBr (001) surface and CeO₂ (111) surface. (c, d) The corresponding calculated electrostatic potentials. (e) Schematic diagram of the formation of the CeO₂/BiOBr composite and the possible charge-separation process in the Z-type heterostructure.

4. Conclusion

In this current work, a novel Z-scheme composite was successfully synthesized by assembling CeO₂ nanoparticles with oxygen vacancies onto the surface of the BiOBr microflowers. Experimental results demonstrated a significant reduction in the photoluminescence intensity, prolonged charge lifetime, and stronger surface photovoltage response in the CeO₂/BiOBr composite. The synergistic effect of oxygen vacancies and the Z-scheme heterojunction in the CeO₂/BiOBr composite effectively facilitates the separation and transfer of photo-generated charge carriers, thereby enhancing the photocatalytic reduction and oxidation performance. This understanding of the Z-scheme mechanism and the charge transfer dynamics in the CeO₂/BiOBr composite paves the way for the development of advanced photocatalytic materials with enhanced performance for environmental and

energy-related applications.

CRediT authorship contribution statement

Juanjuan Sun: Writing – original draft, Visualization, Software, Methodology, Investigation, Data curation, Conceptualization. **Yuxuan Zhang:** Writing – original draft, Visualization, Software, Methodology. **Shiying Fan:** Writing – review & editing, Visualization, Software, Methodology. **Xinyong Li:** Writing – original draft, Supervision, Resources, Formal analysis. **Qidong Zhao:** Writing – review & editing, Visualization, Software, Methodology.

Declaration of Competing Interest

The authors declare that they have no known competing financial

interests or personal relationships that could have appeared to influence the work reported in this paper.

Data availability

Data will be made available on request.

Acknowledgment

This work was supported financially by the National Natural Science Foundation of China (Nos. 22076018), the “Xing Liao Talents Program” Project (XLYC1902051), the Program of Introducing Talents of Discipline to Universities (B13012), the Fundamental Research Funds for the Central Universities (DUT19LAB10), Open foundation of Key Laboratory of Industrial Ecology and Environmental Engineering (KLIEEE-23-06, LTICIEEE-22-0, KLIEEE-22-05), China Ministry of Education, the Program of Natural Science Foundation of Tianjin City (No. 20JCQNJC00670). Additionally, the authors acknowledge the assistance of DUT Instrumental Analysis Center.

Appendix A. Supporting information

Supplementary data associated with this article can be found in the online version at [doi:10.1016/j.apcatb.2024.124248](https://doi.org/10.1016/j.apcatb.2024.124248).

References

- [1] T. Zhang, Y. Jin, S.N. Lou, *Appl. Catal. B Environ. Energy* 353 (2024) 124065.
- [2] S. Yang, Q. Lu, F. Wang, *Chem. Eng. J.* 478 (2023) 147345.
- [3] E.-C. Cho, Y.-S. Hsiao, J.-H. Huang, *J. Taiwan Inst. Chem. Eng.* 149 (2023) 104991.
- [4] Z. Niu, W. Luo, P. Mu, *Sep. Purif. Technol.* 297 (2022) 121513.
- [5] D.P.-H. Tran, M.-T. Pham, Y.-F. Wang, *J. Environ. Chem. Eng.* 11 (2023) 111561.
- [6] K. Aravinthkumar, G. Anandha babu, C. Raja Mohan, *Colloids Surf. A Physicochem. Eng. Asp.* 672 (2023) 131702.
- [7] M. Gao, L. Sun, C. Ma, *Inorg. Chem.* 60 (2021) 1755–1766.
- [8] Z. Zhou, X. Niu, Y. Zhang, *J. Mater. Chem. A* 7 (2019) 21835–21842.
- [9] Y. Gao, L. Sun, J. Bian, *Appl. Surf. Sci.* 610 (2023) 155360.
- [10] J. Geng, S. Guo, Z. Zou, *Fuel* 333 (2023) 126417.
- [11] X. Hu, R.-t. Guo, X. Chen, *J. Environ. Chem. Eng.* 10 (6) (2022) 108582.
- [12] X. Hu, J. Hu, Q. Peng, *Mater. Res. Bull.* 122 (2020) 110682.
- [13] Q. Xu, L. Zhang, J. Yu, *Mater. Today* 21 (2018) 1042–1106.
- [14] B.P. Mishra, K. Parida, *J. Mater. Chem. A* 9 (2021) 10039–11008.
- [15] X. Bao, D. Lu, Z. Wang, *J. Colloid Interface Sci.* 638 (2023) 63–75.
- [16] I. Grigioni, G. Di Liberto, M.V. Dozzi, *ACS Appl. Energy Mater.* 4 (2021) 8421–8431.
- [17] B. Zhang, G. Tan, Z. Wang, *Chem. Eng. J.* 483 (2024) 149384.
- [18] C. Wang, N. Liu, X. Liu, *Chem. Eng. J.* 491 (2024) 151993.
- [19] X. Chen, Y. Wu, Y. Tang, *Chin. Chem. Lett.* 35 (2024) 1109245.
- [20] X.-J. Wen, C. Zhang, C.-G. Niu, *Cat. Commun.* 90 (2017) 51–55.
- [21] X. Chen, Y. Wu, Y. Tang, *Chin. Chem. Lett.* 35 (2023) 1109245.
- [22] C. Zhu, X. Wei, W. Li, *ACS Sustain. Chem. Eng.* 8 (2020), 14397–1440.
- [23] Y. Lu, L. Zhu, C. Agrafiotis, *Prog. Energy Combust. Sci.* 75 (2019) 100785.
- [24] U. Sahoo, S. Pattanayak, S. Choudhury, *Appl. Catal. B Environ.* 343 (2024) 123524.
- [25] J. Sun, X. Li, Q. Zhao, *Appl. Catal. B Environ.* 281 (2021) 119478.
- [26] A. Monshi, M.R. Foroughi, M.R. Monshi, *World J. Nano Sci. Eng.* 2 (2012) 154–160.
- [27] J. Wu, K. Xu, Q. Liu, *Appl. Catal. B Environ.* 232 (2018) 135–145.
- [28] K.A. Alzahrani, A.A. Ismail, N. Alahmadi, *J. Mol. Liq.* 376 (2023) 121509.
- [29] M. Skaf, S. Hany, S. Aouad, *Phys. Chem. Chem. Phys.* 18 (2016), 29381–2938.
- [30] W. Zou, Y. Shao, Y. Pu, *Appl. Catal. B Environ.* 218 (2017) 51–59.
- [31] S. Ali, M. Humayun, W. Pi, *J. Hazard. Mater.* 397 (2020) 122708.
- [32] J. Zhou, X. An, Q. Tang, *Appl. Catal. B Environ.* 277 (2020) 119221.
- [33] Z. Qu, F. Yu, X. Zhang, *Chem. Eng. J.* 229 (2013) 522–532.
- [34] Y. Liu, C. Wen, Y. Guo, *J. Mol. Catal. A Chem.* 316 (2010) 59–64.
- [35] M. Skaf, S. Aouad, S. Hany, *J. Catal.* 320 (2014), 137–14.
- [36] J. Mitra, S. Sarkar, *Inorg. Chem.* 52 (2013) 3032–3042.
- [37] M. Martinezhuerta, *J. Catal.* 225 (2004) 240–248.
- [38] D. Chen, X. Xu, P. Lei, *Colloids Surf. A Physicochem. Eng. Asp.* 672 (2023) 131751.
- [39] Y. Wu, H. Ji, Q. Liu, *J. Hazard. Mater.* 424 (2022) 12756.
- [40] E. Ruiz-Trejo, *J. Phys. Chem. Solids* 74 (2013) 605–610.
- [41] J. Liqiang, Q. Yichun, W. Baiqi, *Sol. Energy Mater. Sol. Cells* 90 (2006), 1773–178.
- [42] S. Kumar, A.K. Ojha, D. Patrice, *Phys. Chem. Chem. Phys.* 18 (2016) 11157–11167.
- [43] J. Liu, J. Zhang, D. Wang, *ACS Sustain. Chem. Eng.* 7 (2019) 12428–12438.
- [44] K. Gao, L.-a. Hou, X. An, *Appl. Catal. B Environ.* 323 (2023) 122150.
- [45] L. Liang, S. Gao, J. Zhu, *Chem. Eng. J.* 391 (2020) 1123599.
- [46] H. Yang, B. Xu, Q. Zhang, *Appl. Catal. B Environ.* 286 (2021) 1119845.
- [47] H. Ji, L. Lyu, L. Zhang, *Appl. Catal. B Environ.* 199 (2016) 230–240.
- [48] H. Li, J. Li, Z. Ai, *Angew. Chem. Int. Ed.* 57 (2018) 122–138.
- [49] K. Wang, X. Yu, Z. Liu, *Chemosphere* 346 (2024) 140596.
- [50] Q. Han, L. Li, W. Gao, *ACS Appl. Mater. Interfaces* 13 (2021) 15092–15100.